Nano Research 2014, 7(9): 1243–1253
DOI 10.1007/s12274-014-0487-y
Research Article
ISSN 1998-0124
CN 11-5974/O4

Te-seeded growth of few-quintuple layer Bi_2Te_3 nanoplates

Yanyuan Zhao[1], Maria de la Mata[2], Richard L. J. Qiu[3], Jun Zhang[1], Xinglin Wen[1], Cesar Magen[4], Xuan P. A. Gao[3], Jordi Arbiol[2,5] (✉), and Qihua Xiong[1,6] (✉)

[1] *Division of Physics and Applied Physics, School of Physical and Mathematical Sciences, Nanyang Technological University, Singapore 637371*
[2] *Institut de Ciència de Materials de Barcelona, ICMAB-CSIC, E-08193 Bellaterra, CAT, Spain*
[3] *Department of Physics, Case Western Reserve University, Cleveland, Ohio 44106, USA*
[4] *Laboratorio de Microscopías Avanzadas (LMA), Instituto de Nanociencia de Aragon (INA) - ARAID and Departamento de Fisica de la Materia Condensada, Universidad de Zaragoza, 50018 Zaragoza, Spain*
[5] *Institució Catalana de Recerca i Estudis Avançats (ICREA), 08010 Barcelona, CAT, Spain*
[6] *NOVITAS, Nanoelectronics Centre of Excellence, School of Electrical and Electronic Engineering, Nanyang Technological University, Singapore 639798*

Received: 16 February 2014
Revised: 26 April 2014
Accepted: 27 April 2014

KEYWORDS
Te nucleation seed, epitaxial growth, Bi_2Te_3, few-quintuple layer, TEM cross-section, optical contrast

ABSTRACT

We report on a Te-seeded epitaxial growth of ultrathin Bi_2Te_3 nanoplates (down to three quintuple layers (QL)) with large planar sizes (up to tens of micrometers) through vapor transport. Optical contrast has been systematically investigated for the as-grown Bi_2Te_3 nanoplates on the SiO_2/Si substrates, experimentally and computationally. The high and distinct optical contrast provides a fast and convenient method for the thickness determination of few-QL Bi_2Te_3 nanoplates. By aberration-corrected scanning transmission electron microscopy, a hexagonal crystalline structure has been identified for the Te seeds, which form naturally during the growth process and initiate an epitaxial growth of the rhombohedral-structured Bi_2Te_3 nanoplates. The epitaxial relationship between Te and Bi_2Te_3 is identified to be perfect along both in-plane and out-of-plane directions of the layered nanoplate. Similar growth mechanism might be expected for other bismuth chalcogenide layered materials.

1 Introduction

Two-dimensional (2D) crystals have attracted tremendous interest in the past few years for their richness in unusual physical and chemical properties and the potentials of novel applications [1]. 2D crystals exist in many categories of layered materials, including graphite, boron nitride, vanadium oxide, a large family

Address correspondence to Jordi Arbiol, arbiol@icrea.cat; Qihua Xiong, qihua@ntu.edu.sg

of transition metal dichalcogenides, and some group III, IV, and V metal chalcogenides [1–3]. Bi_2Te_3 is an important layered compound which has been historically well known for its excellent thermoelectric properties [4]. Recently, Bi_2Te_3, together with Bi_2Se_3 and Sb_2Te_3, have been shown to be 3D topological insulators, a new state of quantum matter which has insulating bulk states but conducting surface states that are robust against any nonmagnetic disorder scatterings [5–7]. The intriguing surface states make topological insulators promising for unprecedented applications in spintronics, low-power electronics and quantum computing [8, 9]. Topological insulator nanostructures, especially 2D crystals, are advantageous compared to their bulk counterparts because of (1) the enhanced surface state contribution due to the extremely large surface-to-volume ratio, and (2) the enlarged bulk band gap caused by quantum size effect, which allows wider operation ranges for spintronic devices. Angular-resolved photoemission spectroscopy (ARPES) demonstrated that in the 2D limit, the nontrivial topological insulators would turn to trivial insulators [10, 11]. Recent transport measurements on topological insulator thin films and nanostructures have reported the ambipolar field effect, Aharonov–Bohm (AB) effect and Shubnikov–de Haas (SdH) oscillations that are associated with the surface states [12–16]. The thermoelectric performance has also been demonstrated to be largely enhanced in the ultrathin nanoplate-formed Bi_2Te_3/Bi_2Se_3 binary or ternary compounds due to the strong anisotropy [17–21]. Thus, the synthesis of high-quality ultrathin bismuth chalcogenide topological insulator 2D crystals is highly important for both the fundamental investigations and technological applications.

Most of the synthesized Bi_2X_3 (X = Se, Te) nanostructures apprear in two dimensional forms (nanobelt, nanoplate, nanofilm) because of their layered crystal structure with rhombohedral symmetry (D_{3d}^5) [22]. Five atomic layers (X–Bi–X–Bi–X) are covalently bonded, forming one non-polar quintuple layer (QL) with a thickness of around 1 nm. Adjacent QLs are weakly coupled via the weak van der Waals interactions and hence easy cleavage is allowed perpendicular to the *c* axis along which the QLs pile up. Bi_2X_3 2D crystals have been produced through a variety of methods, such as mechanical exfoliation [23, 24], molecular beam epitaxy (MBE) [25], vapor transport [26–29], and chemical solution synthesis [17, 19, 21, 30]. Vapor transport is cost-effective, contamination-free, and feasible to achieve ultrathin Bi_2X_3 thin films. Different choices of substrates can lead to diverse products during the vapor transport process. Oriented Bi_2X_3 nanoplate arrays have been prepared on mica and graphene through van der Waals epitaxy [27, 28, 31]. Si substrates have been commonly adopted for the synthesis of Bi_2X_3 nanostructures with diverse morphologies [32]. Inspired by the good optical contrast in the graphene/SiO_2/Si system [33], Si substrates capped with an oxide layer might enable the visibility and easy location of few-QL Bi_2X_3 crystals under optical microscope. Besides, SiO_2/Si substrates are also favorable for *in situ* field effect transistor (FET) device fabrication. Despite a large number of reports on vapor transport grown Bi_2X_3 2D crystals, a comprehensive investigation of the growth mechanism—which is important in terms of controllable synthesis, structural design and functional engineering—is still needed. Here, we report the synthesis of few-QL Bi_2Te_3 (down to 3-QL) nanoplates and reveal a Te-seeded epitaxial growth process, supported by a comprehensive characterization using optical and transmission electron microscopy and spectroscopy. The optical contrast of few-QL Bi_2Te_3 nanoplates on SiO_2/Si substrates has been investigated, and provides a fast and convenient approach for the thickness determination.

2 Results and discussion

Bi_2Te_3 nanoplates were synthesized in a home-built vapor transport system (see Methods) [34, 35]. Figure 1(a) shows the bright field optical images of as-grown Bi_2Te_3 nanoplates on the 100 nm SiO_2/Si substrates. Most nanoplates exhibit hexagonal, triangular, or truncated triangular shapes with lateral sizes from several microns up to tens of microns. The typical thickness is about a few nanometers and the thinnest we could achieve is 3 nm, corresponding to 3-QL. It is worth noting that a bright dot-like feature is found in the center of many nanoplates, as can be clearly seen in the dark field image (Fig. 1(b)). Atomic

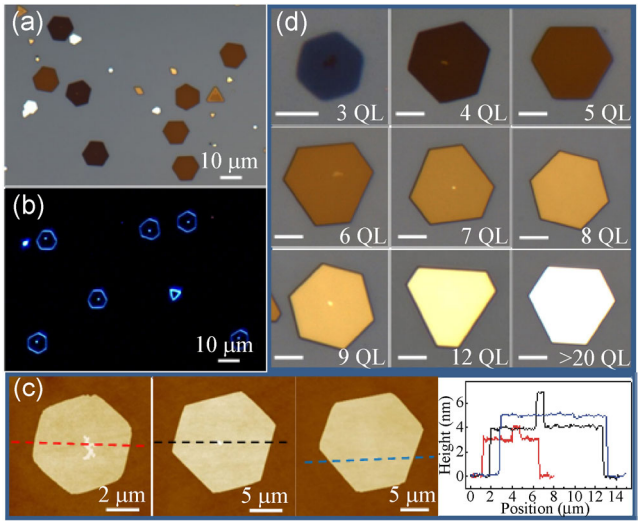

Figure 1 (a) Bright field optical image of as-grown Bi_2Te_3 nanoplates on 100 nm SiO_2/Si substrates. Nanoplates of various thicknesses show different colors in the bright field image. (b) Dark field optical image of as-grown Bi_2Te_3 nanoplates. A bright spot can be seen in the center of many nanoplates, which works as the nucleation seed to initiate the nanoplate growth. (c) AFM images of 3-QL, 4-QL and 5-QL Bi_2Te_3 nanoplates. The thickness profiles are taken from the corresponding colored dashed lines. (d) Optical images of Bi_2Te_3 nanoplates with thicknesses from 3 QLs to more than 20 QLs. All the scale bars in (d) are 5 μm.

force microscopy (AFM) measurements indicate that the bright dot is thicker than the rest of the nanoplates (Fig. 1(c)). The central features were further investigated by scanning electron microscopy (SEM) and found to possess a particle or thin film morphology (see Fig. S1 in the Electronic Supplementary Material (ESM)), likely corresponding to the nucleation center and a growing top layer, respectively. The as-grown nanoplates exhibit different colors under the optical microscope, an indication of different thicknesses, similar to the case for other 2D crystals [36, 37]. Extensive AFM measurements confirm a one-to-one correlation between the colors and thicknesses. Figure 1(d) shows the bright field optical images of 3–9-QL and even thicker Bi_2Te_3 nanoplates. The colors (optical contrasts) for 8-QL and below are very distinct for each thickness and can be easily distinguished by eye. The excellent optical contrast for few-QL Bi_2Te_3 provides a quick and convenient approach for the nanoplate location and thickness identification under the optical microscope, which is useful for further optical characterizations and electronic device fabrications.

Optical contrast in the three-layer thin film system (Bi_2Te_3/SiO_2/Si, Fig. 2(a)) originates from the interference of the reflected light from different interfaces. The presence of the opaque Bi_2Te_3 thin film adds an optical path, changing its interference color with respect to the empty SiO_2/Si substrates [33]. The optical contrast of Bi_2Te_3 thin flakes has previously been studied by

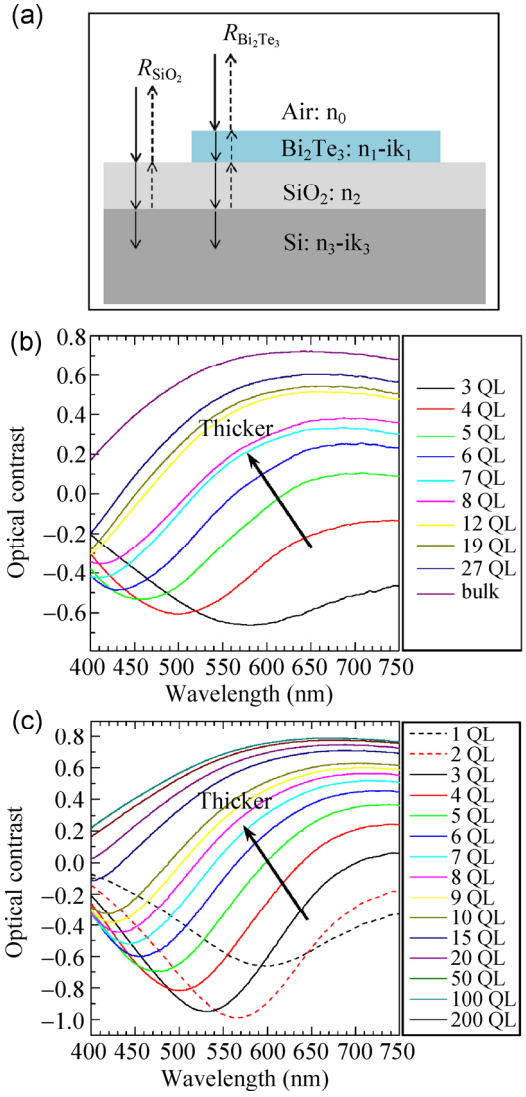

Figure 2 (a) Schematic of the optical reflection and transmission with normal incidence in the three-layer thin film system. Solid lines indicate the incident light and dashed lines stand for the reflected light. (b) Measured optical contrast spectra of as-grown few-QL Bi_2Te_3 nanoplates on 100 nm SiO_2/Si substrates. (c) Calculated optical contrast of Bi_2Te_3 thin films with thicknesses from 1-QL to bulk. The spectra for 1-QL and 2-QL are shown in dashed lines while those for 3-QL and above are in solid lines.

Li et al., in which they focused on the contrast optimization under different illumination wavelengths, while the experimental contrast data of few-QLs were not comprehensively presented [38]. In our study, we demonstrate a distinctive optical contrast under white light illumination for each thickness in the few-QL regime, experimentally and theoretically. The optical contrast of the Bi_2Te_3 nanoplates can be quantitatively represented by the Michelson contrast [39]

$$\text{optical contrast} = \frac{R_{Bi_2Te_3} - R_{SiO_2}}{R_{Bi_2Te_3} + R_{SiO_2}},$$

where $R_{Bi_2Te_3}$ is the reflected light intensity from the nanoplate and R_{SiO_2} is that from the bare SiO_2/Si substrates, both of which can be measured via a micro-reflection spectrometer (Craic 20) in our experiments. The value of optical contrast ranges from –1 to 1, where the positive (negative) sign indicates a stronger (weaker) reflection from the Bi_2Te_3 nanoplate than from the substrates. Figure 2(b) displays the measured optical contrast spectra in the visible region (400–750 nm) for few-QL and bulk Bi_2Te_3 nanoplates. A contrast minimum can be seen in the spectra for 3–8-QL, exhibiting a blue shift while increasing the thickness, as denoted by the arrow. For even thicker nanoplates (12-QL and above), the contrast minimum probably shifts out of the visible region and cannot be identified. The 3-QL and 4-QL nanoplates exhibit negative optical contrast through the whole visible region, consistent with the fact that they appear darker than the substrates in the optical images. From 5-QL, the positive contrast becomes more and more dominant with increased thickness and covers the whole visible range in the limit of bulk, explaining why thicker nanoplates appear brighter to the eye under the optical microscope.

To explain the observed optical contrast in our Bi_2Te_3/SiO_2/Si system, calculations were carried out based on Fresnel's equations with a simple normal incidence geometry (as shown in Fig. 2(a)) [33]. The refractive indices of the four media (air, Bi_2Te_3, SiO_2, and Si) required for the calculations were obtained from the literature [40–42]. The calculated optical contrasts for 1–200-QL Bi_2Te_3 on 100 nm SiO_2/Si substrates are shown in Fig. 2(c). The contrast spectra for 50-QL and above are identical, indicating that a 50-QL Bi_2Te_3 nanoplate should appear the same as the bulk crystal. The calculated results show a blue shift of the contrast minimum as the thickness increases, qualitatively in agreement with the experiments. Quantitatively, the experimental and calculated results are in good agreement for bulk Bi_2Te_3 but not for few-QL nanoplates. This discrepancy indicates that the refractive index of few-QL Bi_2Te_3 might be different from that of their bulk counterpart, given that the refractive index of bulk Bi_2Te_3 was used in the calculations for all thicknesses. Another factor that could contribute to the discrepancy is the simplified normal incidence model employed for our contrast calculations, while in the experiments an objective with numerical aperture of 0.5 was used. A more complex model [39] considering the incident light angle might be able to characterize our system better but it is beyond the scope of this manuscript. The thickness of the SiO_2 layer is the key factor determining the optical contrast in the Bi_2Te_3/SiO_2/Si system. Our calculations found that 100 nm SiO_2 gives the highest contrast under visible illumination for few-QL Bi_2Te_3 (see Fig. S2 in the ESM), consistent with previous calculated results for the same system [38].

A detailed scanning transmission electron microscopy (STEM) characterization has been conducted on the Bi_2Te_3 nanoplates. A polymethyl methacrylate (PMMA) transfer method was used for the TEM sample preparation (see the Methods section). Figure 3 shows the released Bi_2Te_3 samples on lacey carbon studied under aberration corrected high-angle annular dark-field (HAADF) STEM conditions. The image contrast is proportional to the nanoplate thickness, where the brighter hexagon (Fig. 3(a)) is thicker than the darker one (Fig. 3(b)). The nanoplates crystallize in the tellurobismuthite ($R\bar{3}m$) phase with the hexagonal facets corresponding to the $\{01\bar{1}0\}$ planes, and the growth direction is along the [0001] axis perpendicular to the hexagon plane, as identified from the selected-area electron diffraction (SAED) pattern (Fig. 3(c)). It is worth noting that small holes were found in the center of the nanoplate and notches on the edges. The notches on the edges were probably caused by the accidental damage during the sample preparation process. Cheng et al. have reported similar center-hollowed Bi_2Te_3 nanoplates broken from T-shaped

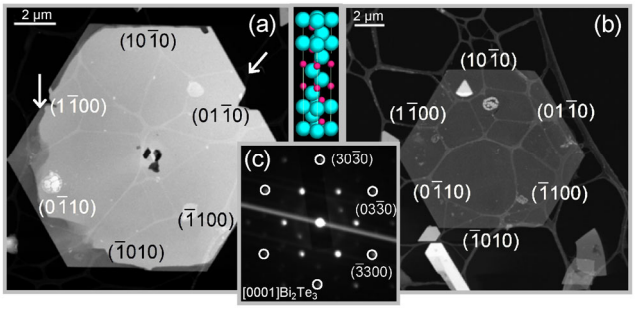

Figure 3 HAADF STEM images of two hexagonal Bi_2Te_3 nanoplates on lacey carbon. The image contrast is proportional to the plate thickness. (a) A thicker nanoplate with holes in the center, where the seed was located. (b) A thinner nanoplate. The nanoplates crystallize in the tellurobismuthite ($R\bar{3}m$) phase. The facets of the hexagons are {01$\bar{1}$0} planes, as observed from the SAED pattern in (c).

Bi_2Te_3(nanoplate)–Te(nanorod) heterojunctions [43]. In our as-prepared TEM samples, the hole features were commonly present in the released Bi_2Te_3 nanoplates and we tentatively propose that they might be related to the nucleation seeds (bright spots in Fig. 1), which are left over during the release process, causing the holes in the released nanoplates.

To further characterize the possible nucleation seeds in the center of the Bi_2Te_3 nanoplates, planar view TEM samples were prepared from the as-grown Bi_2Te_3 nanoplates on SiO_2/Si substrates by thinning the backside of the substrates using conventional electron microscopy sample preparation methods. Figure 4(a) shows the HAADF STEM image of a typical nanoplate with truncated triangular morphology from the studied area (Fig. 4(c)) and its surface plot is presented in Fig. 4(b). A darker contrast (denoted by the black square in Fig. 4(a) and the orange square in Fig. 4(b)) was revealed in the nanoplate, and is clearly shown in the intensity profile along the direction indicated by the black arrow (Fig. 4(d)). The contrast difference can be due to a thickness change or to a compositional variation. The HRTEM analysis of this darker contrast region shows a particle-like agglomerate with a size of around 50 nm (Fig. 4(e)), which is likely to correspond to the nucleation seeds that appear as bright dots in the Bi_2Te_3 nanoplates under the optical microscope (see Fig. 1). Through the study of the fast Fourier transform (FFT) (Fig. 4(f)) of the image Fig. 4(e), we can identify not only the Bi_2Te_3 and the Si phases, but also a hexagonal tellurium phase ($P3_121$). The appearance of the Te phase can explain the darker contrast region in Fig. 4(a), since the image intensity is proportional to the square of the atomic number (Z^2_{Bi} = 6,889; Z^2_{Te} = 2,704). Moreover, the Te phase shows a (11$\bar{2}$0) [0001] Te // (11$\bar{2}$0) [0001] Bi_2Te_3 epitaxial relationship with the Bi_2Te_3 phase, as denoted in Fig. 4(f). Notice that the green hexagon in

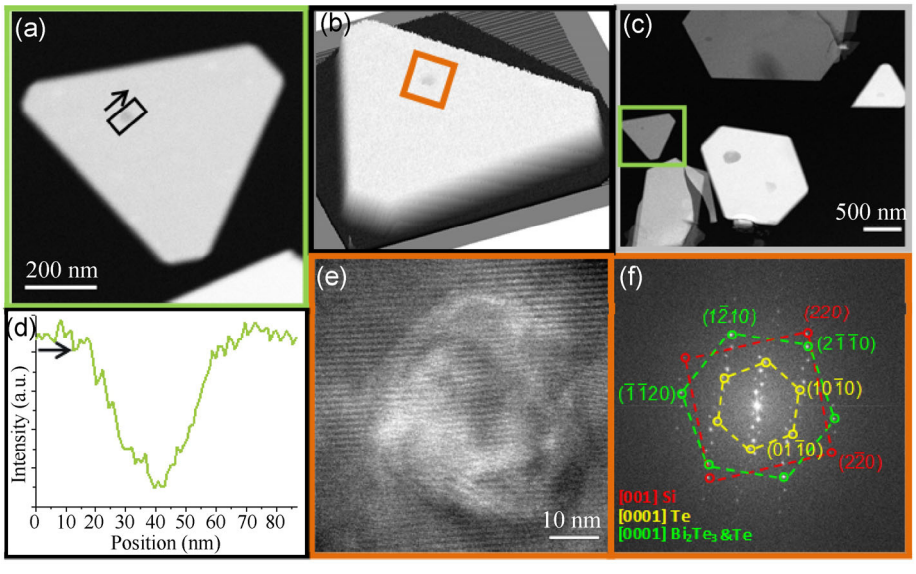

Figure 4 Planar view of Bi_2Te_3 nanoplates on SiO_2/Si substrates. (a) HAADF of the studied nanoplate. (b) Surface plot of the plate in (a). (c) Low magnification HAADF image of the studied area. (d) Intensity profile taken from the black square in (a) along the arrow indicated direction. (e) HRTEM image of the darker feature in the region marked with a black square in (a). (f) FFT of image (e).

Fig. 4(f) represents the $\{1\bar{2}10\}$ lattice planes of both the Bi_2Te_3 and Te phases while the yellow hexagon only represents the $\{10\bar{1}0\}$ planes of Te, in agreement with our simulated diffraction patterns (Fig. S3 in the ESM). The epitaxial relationship between Te and Bi_2Te_3 can be further identified as perfect epitaxy along the *c* axis since the in-plane lattice mismatch is only 1.6% for the Te (a = 4.447 Å) and Bi_2Te_3 (a = 4.375 Å) phases [44], in agreement with previous reports on the Bi_2Te_3/Te heterostructures [43, 45]. The crystalline Te phase and the Te/Bi_2Te_3 epitaxy have also been observed in several other Bi_2Te_3 nanoplates in the studied area (Fig. 4(c)).

The appearance of the Te phase in the Bi_2Te_3 nanoplates can be understood from analyzing the detailed vapor transport growth process—Bi_2Te_3 sublimation and recrystallization. Early measurements on the vapor pressure of crystalline Bi_2Te_3 indicated that the sublimation occurred congruently below the melting temperature 585 °C, following the decomposition reaction $Bi_2Te_3\,(s) \rightarrow 2BiTe\,(g) + 1/2\,Te_2\,(g)$ [46–48], while later Brebrick et al. cast doubt on the validity of the proposed reaction for an equilibrium sublimation and suggested an incongruent sublimation process with Te-rich (atomic percent > 60%) vapor species [49]. A Te-rich composition will lead to a phase segregation during the crystallization process and thus the formation of two equilibrium crystalline phases, Bi_2Te_3 and Te, according to the Bi-Te binary phase diagram [50]. During the vapor transport growth, BiTe and Te_2 molecules (the major vapor species) subliming from the Bi_2Te_3 powder source are carried with the gas flow to a lower temperature zone and deposit on the substrates into Bi_2Te_3 nanoplates, according to the synthesis reaction $2BiTe\,(g) + 1/2\,Te_2\,(g) \rightarrow Bi_2Te_3\,(s)$. The wide presence of the Te crystalline seeds in as-grown Bi_2Te_3 nanoplates implies an excess of the Te_2 molecules in the sublimed vapor species, in agreement with the report from Brebrick et al. [49]. The identification of the Te/Bi_2Te_3 epitaxial relationship as elucidated by transmission electron microscopy, suggests a Te-seeded epitaxial growth of Bi_2Te_3 nanoplates in our vapor transport process.

To further examine the epitaxial growth mechanism proposed, cross-section samples have been analyzed under HAADF STEM conditions by using an aberration-corrected microscope. Figure 5(a) shows a HAADF STEM image of a nanoplate with thickness of around 300 nm, along with its surface plot below to show the nanoplate morphology. Electron energy loss spectroscopy (EELS) analysis was performed to study the elemental constitution of the nanoplate and the mapping results are presented as Fig. 5(b). The bright cyan color on the right side of the nanoplate corresponds to a pure Te structure aggregated at the lateral facet of the plate. Furthermore, it was found that the Te phase exists in the pinholes in the SiO_2 layer until it reaches the Si substrate, while the Bi signal is restricted only to the nanoplate. Figure 5(c) (the region marked by a pink square in Fig. 5(a)) shows the atomic resolution HAADF STEM image of the interface between the Bi_2Te_3 nanoplate and the SiO_2 layer of the substrates, where five atomic layers Te–Bi–Te–Bi–Te can be identified as a QL (the Bi and Te atoms are highlighted as pink and cyan dots, respectively). Between the bottom QL of the Bi_2Te_3 nanoplate and the SiO_2 substrates, three atomic layers of Te can be seen. A van der Waals gap can be identified between the Te phase and the bottom Bi_2Te_3 QL, implying the lowest interface energy in this case. Again, the perfect epitaxial relationship can be directly identified between the Te atomic layers and the bottom QLs of the Bi_2Te_3 nanoplate along the *c* axis. The Te crystalline layer at the interface is only present in the pinhole region and should be closely related to the Te nucleation seed as discussed above. We tentatively propose that most of the Te nucleation happens at the pinhole pits, since thermodynamically the substrate imperfections could facilitate the heterogeneous nucleation by vapor condensation [52]. The pinhole features embedded in the SiO_2 layer may result in an attachment between the nucleation seed and the Si substrates. During the nanoplate releasing process through HF etching, the SiO_2 layer gets etched away following the reaction $SiO_2 + 4HF \rightarrow SiF_4\,(g) + 2H_2O$, while the Te pinhole remains. The Te seed might be torn away from the rest of the nanoplate due to its attachment to the Si substrate, thus leaving a hole feature in some released Bi_2Te_3 nanoplates (Fig. 3(a)).

Figure 5(d) (the region marked with a blue square in Fig. 5(a)) displays the atomic resolution interface between the Bi_2Te_3 nanoplate and the laterally attached

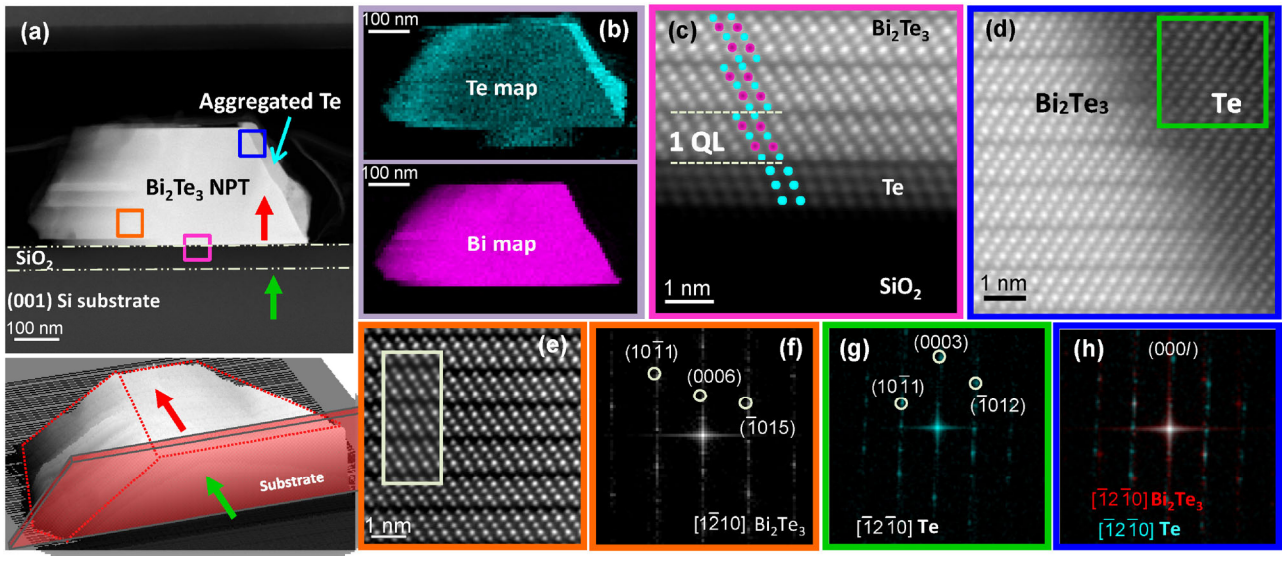

Figure 5 STEM cross-section analysis of an as-grown Bi_2Te_3 nanoplate on a SiO_2/Si substrate. (a) HAADF STEM image of the nanoplate studied, also displayed as a surface plot below. The colored frames indicate the regions where the atomic resolution HAADF STEM analyses were performed. (b) Mapping of the EELS Te signal (cyan colored) and Bi signal (pink colored). (c) Bottom interface between the Bi_2Te_3 nanoplate and SiO_2/Si substrate taken in the region marked with a pink square in (a), showing a few pure Te layers in between. One QL of Bi_2Te_3 is denoted by the white dashed lines. (d) Interface between the Bi_2Te_3 nanoplate and the attached Te structure on the lateral side, taken in the region marked with a blue square in (a). (e) Atomic resolution HAADF STEM image of the Bi_2Te_3 structure, taken in the region marked with an orange square in (a). The inset corresponds to the simulated structure by using the STEM-CELL software [51]. (f) FFT of (e). (g) FFT of the Te aggregation, in the area marked by the green square in (d). (h) FFT of (d), showing the epitaxy between the Bi_2Te_3 and the Te aggregation.

Te structure, where an imperfect epitaxial relationship can be observed with the presence of some misfit dislocations at the interface. This epitaxial relationship can be further studied from the FFT analysis of the regions marked with blue and green squares as (0001) [$\bar{1}2\bar{1}0$] Bi_2Te_3 // (0001) [$\bar{1}2\bar{1}0$] Te (see Figs. 5(g) and 5(h)), with a slight angle between the (0001) planes of the two phases. The lattice mismatch along the *c* axis between the Te and Bi_2Te_3 phases is around 2.7% (*c* = 30.39 Å for Bi_2Te_3; *c* = 5.92 Å for Te) [44], and a perfect in-plane epitaxy is expected for such a small mismatch, as the case out of plane. The observed imperfect in-plane epitaxy can be explained by the inhomogeneity of Bi_2Te_3 along the *c* axis. The atomic layers are evenly spaced along the *c* axis in Te but not in Bi_2Te_3 due to the presence of the van der Waals gaps. In fact, 2.7% is underestimating the lattice mismatch assuming an even atomic-layer spacing along the *c* axis for both Bi_2Te_3 and Te, and the misfit dislocations observed at the interface can be attributed to a real lattice mismatch that is much bigger. At more than a few nanometers from the interface, the Te phase relaxes from the strain caused by the interface and aligns perfectly in plane with the Bi_2Te_3 phase. Thus far, an epitaxial relationship between the six-fold symmetry Te ($P3_121$) and Bi_2Te_3 ($R\bar{3}m$) phases has been confirmed both along and perpendicular to the *c* axis. It is worth noting that two different Bi_2Te_3 crystalline orientations were observed in the region marked with an orange square (Fig. 5(e)) and the region marked with a blue square (Fig. 5(d)), indicating the presence of a twin boundary somewhere in between. In polycrystalline Bi_2Te_3, (0001) basal twin boundaries have been observed with a termination at the van der Waals gaps between two adjacent QLs [53, 54]. This twin boundary configuration has also been confirmed to be energetically favorable, according to ab initio calculations [53]. Therefore, we believe that the same (0001) basal twin boundary also presents in the nanoplate studied here. Considering the fact that the crystalline orientation keeps the same in a range of tens of QLs (between the orange and pink regions), we assume that twin boundaries are unlikely to be present in the case of few-QL nanoplates.

The nanoplate studied in Fig. 5 represents a percentage of as-grown nanoplates where the central Te nucleation seeds cannot be identified from the top-view optical and STEM images. Note that during the vapor transport growth, the volume of both Bi_2Te_3 and Te crystalline phases will gradually increase with a continuous Te-rich vapor supply and condensation, as a result of the Bi_2Te_3–Te phase segregation, as discussed above. In the condition of fast Bi_2Te_3 phase formation, the central Te seed might get merged in the Bi_2Te_3 nanoplate. Consequently, the growth of the nucleation seed will be cut off by the lack of Te supply. Instead, the excess Te adatoms will crystallize into a new Te crystalline phase on the surface of the nanoplate, corresponding to the Te aggregation shown in Fig. 5(b). We tentatively believe that extra Te aggregation is most likely to form on large and thick nanoplates, where the nanoplate growth is more rapid and larger quantities of the Te phase are expected, in comparison with the few-QL cases.

Thus, by combining all the above characterization methods (optical microscopy, AFM, SEM, and aberration corrected HAADF STEM), we propose a nanoplate growth model: During the early growth stages, the Te-rich vapor species that sublime from Bi_2Te_3 powder source condensate on the substrates (preferentially at the pinhole locations), forming Te crystalline seeds. During the condensation process, some vapor is inclined to diffuse through the SiO_2 pinholes and then solidify, resulting in an attachment between the nucleation seeds and the Si substrates. Meanwhile, the BiTe and Te_2 vapors become adsorbed to the Te nucleation seeds and react to form Bi_2Te_3, which grows epitaxially into nanoplates. The epitaxial growth occurs both laterally and vertically, following a layer-by-layer manner. The thickness of the nanoplate is determined by the size of the nucleation seed as well as the supply of BiTe and Te_2 vapors. The absence of the nucleation seeds in some nanoplates suggests that the Te seeds either become merged into the Bi_2Te_3 nanoplates due to the fast growth process, or react with BiTe vapor and are completely converted to Bi_2Te_3.

3 Conclusions

Few-QL topological insulating Bi_2Te_3 nanoplates with large planar sizes have been synthesized through vapor transport. Optical contrast in the $Bi_2Te_3/SiO_2/Si$ system was systematically studied both experimentally and computationally. The high optical contrast provided by the 100 nm SiO_2/Si substrates provides a fast and convenient approach for the location and thickness determination of few-QL Bi_2Te_3 nanoplates. The nanoplate growth mechanism has been comprehensively investigated and a Te-seeded growth model was revealed, where crystalline Te seeds firstly form thermodynamically and then initiate the epitaxial growth of the Bi_2Te_3 nanoplates. The epitaxial relationship between Bi_2Te_3 and Te can be taken advantage of in different types of growth methods, shedding light on the potential growth of the Bi_2Te_3/Te superlattices. This simple and effective growth mechanism might be extended to the growth of other topological insulator thin films like Bi_2Se_3 and Sb_2Te_3.

4 Methods

4.1 Vapor transport growth

The Bi_2Te_3 nanoplates were synthesized in a 2-inch quartz tube placed inside a tube furnace (Lindberg/Blue M) [34, 35]. Bi_2Te_3 power (99.99%, Alfa Aesar) was positioned in the center of the quartz tube during the growth. Commercial (100) Si substrates capped with a 100 nm thermal oxidized layer were cleaned by isopropyl alcohol and placed around 15 cm downstream from the powder source during the growth. The growth chamber was firstly evacuated to ~5 mTorr and then flushed several times with the carrier gas (Ar or H_2). The nanoplate growth was conducted at 480 ˚C with a 30 sccm, 100 Torr Ar/H_2 flow for 10 min. The adoption of Ar or H_2 as carrier gas gives similar growth products.

4.2 Bi_2Te_3 nanoplate release

SiO_2/Si substrates with as-grown Bi_2Te_3 nanoplates on top were firstly spin coated a layer of PMMA with a thickness of around 300 nm and then baked at 180 ˚C for 5 min. After immersing the PMMA coated substrates in buffered HF solution for a few hours, the SiO_2 layer was etched away and the PMMA film with Bi_2Te_3 nanoplates embedded in was released from the Si substrates. The PMMA film was then rinsed off

using deionized water and transferred to TEM grids covered with lacey carbon. PMMA was then removed by acetone, leaving Bi_2Te_3 nanoplates on the lacey carbon.

4.3 Planar and cross-section STEM sample preparation

The cross-section samples were prepared by gluing two pieces of substrate containing the grown nanoplates, and placing the nanoplates face-to-face. Then, conventional polishing was laterally performed to obtain a sample around 20 μm thick, which was then attached to a copper grid. Finally, precision ion polishing was carried out in a precision ion polishing system (PIPS) to obtain an electron-transparent sample.

Acknowledgements

Q. X. gratefully acknowledges the strong support of this work by the Singapore National Research Foundation through a fellowship grant (NRF-RF2009-06). This work was also supported in part by Ministry of Education via a Tier 2 grant (MOE2011-T2-2-051), start-up grant support (M58113004) and New Initiative Fund (M58110100) from Nanyang Technological University (NTU). MdlM thanks CSIC JAE-Predoc program. J. A. acknowledges the funding from the Spanish MICINN project MAT2010-15138 (COPEON) and Generalitat de Catalunya (2014 SGR 1638). The authors thank the TEM facilities at INA-LMA at University of Zaragoza, and F. J. Belarre for TEM sample preparation (planar and X-section). X. P. A. G. thanks the NSF CAREER Award program (DMR-1151534) for funding support.

Electronic Supplementary Material: Supplementary material (further details of SEM images, optical contrast calculations and simulations of diffraction patterns) is available in the online version of this article at http://dx.doi.org/10.1007/s12274-014-0487-y.

References

[1] Butler, S. Z.; Hollen, S. M.; Cao, L.; Cui, Y.; Gupta, J. A.; Gutiérrez, H. R.; Heinz, T. F.; Hong, S. S.; Huang, J.; Ismach, A. F.; et al. Progress, challenges, and opportunities in two–dimensional materials beyond graphene. *ACS Nano* **2013**, *7*, 2898–2926.

[2] Koski, K. J.; Cui, Y. The new skinny in two–dimensional nanomaterials. *ACS Nano* **2013**, *7*, 3739–3743.

[3] Feng, J.; Sun, X.; Wu, C. Z.; Peng, L. L.; Lin, C. W.; Hu, S. L.; Yang, J. L.; Xie, Y. Metallic few-layered VS_2 ultrathin nanosheets: High two-dimensional conductivity for in-plane supercapacitors. *J. Am. Chem. Soc.* **2011**, *133*, 17832–17838.

[4] Nolas, G. S.; Sharp, J.; Goldsmid, H. J. *Thermoelectrics: Basic Principles and New Materials Developments*; Springer: New York, 2001.

[5] Zhang, H. J.; Liu, C.-X.; Qi, X.-L.; Dai, X.; Fang, Z.; Zhang, S.-C. Topological insulators in Bi_2Se_3, Bi_2Te_3 and Sb_2Te_3 with a single Dirac cone on the surface. *Nat. Phys.* **2009**, *5*, 438–442.

[6] Xia, Y.; Qian, D.; Hsieh, D.; Wray, L.; Pal, A.; Lin, H.; Bansil, A.; Grauer, D.; Hor, Y. S.; Cava, R. J.; et al. Observation of a large–gap topological–insulator class with a single Dirac cone on the surface. *Nat. Phys.* **2009**, *5*, 398–402.

[7] Hasan, M. Z.; Kane, C. L. Colloquium: Topological insulators. *Rev. Mod. Phys.* **2010**, *82*, 3045.

[8] Žutić, I.; Fabian, J.; Das Sarma, S. Spintronics: Fundamentals and applications. *Rev. Mod. Phys.* **2004**, *76*, 323–410.

[9] Moore, J. Topological insulators: The next generation. *Nat. Phys.* **2009**, *5*, 378–380.

[10] Zhang, Y.; He, K.; Chang, C.-Z.; Song, C.-L.; Wang, L.-L.; Chen, X.; Jia, J.-F.; Fang, Z.; Dai, X.; Shan, W.-Y. Crossover of the three-dimensional topological insulator Bi_2Se_3 to the two-dimensional limit. *Nat. Phys.* **2010**, *6*, 584–588.

[11] Liu, Y.; Bian, G.; Miller, T.; Bissen, M.; Chiang, T. C. Topological limit of ultrathin quasi-free-standing Bi_2Te_3 films grown on Si(111). *Phys. Rev. B* **2012**, *85*, 195442.

[12] Peng, H. L.; Lai, K. J.; Kong, D. S.; Meister, S.; Chen, Y. L.; Qi, X.-L.; Zhang, S.-C.; Shen, Z.-X.; Cui, Y. Aharonov–Bohm interference in topological insulator nanoribbons. *Nat. Mater.* **2010**, *9*, 225–229.

[13] Xiu, F. X.; He, L.; Wang, Y.; Cheng, L.; Chang, L.-T.; Lang, M.; Huang, G.; Kou, X. F.; Zhou, Y.; Jiang, X. W.; et al. Manipulating surface states in topological insulator nanoribbons. *Nat. Nanotechnol.* **2011**, *6*, 216–221.

[14] Kong, D. S.; Chen, Y. L.; Cha, J. J.; Zhang, Q. F.; Analytis, J. G.; Lai, K. J.; Liu, Z. K.; Hong, S. S.; Koski, K. J.; Mo, S.-K.; et al. Ambipolar field effect in the ternary topological insulator $(Bi_xSb_{1-x})_2Te_3$ by composition tuning. *Nat. Nanotechnol.* **2011**, *6*, 705–709.

[15] Yuan, H. T.; Liu, H. W.; Shimotani, H.; Guo, H.; Chen, M. W.; Xue, Q. K.; Iwasa, Y. Liquid-gated ambipolar transport

in ultrathin films of a topological insulator Bi_2Te_3. *Nano Lett.* **2011**, *11*, 2601–2605.

[16] Wang, Z. H.; Qiu, R. L. J.; Lee, C. H.; Zhang, Z.; Gao, X. P. A. Ambipolar surface conduction in ternary topological insulator $Bi_2(Te_{1-x}Se_x)_3$ nanoribbons. *ACS Nano* **2013**, *7*, 2126–2131.

[17] Min, Y.; Roh, J. W.; Yang, H.; Park, M.; Kim, S. I.; Hwang, S.; Lee, S. M.; Lee, K. H.; Jeong, U. Surfactant-free scalable synthesis of Bi_2Te_3 and Bi_2Se_3 nanoflakes and enhanced thermoelectric properties of their nanocomposites. *Adv. Mater.* **2013**, *25*, 1425–1429.

[18] Soni, A.; Yanyuan, Z.; Ligen, Y.; Aik, M. K. K.; Dresselhaus, M. S.; Xiong, Q. H. Enhanced thermoelectric properties of solution grown $Bi_2Te_{3-x}Se_x$ nanoplatelet composites. *Nano Lett.* **2012**, *12*, 1203–1209.

[19] Son, J. S.; Choi, M. K.; Han, M.-K.; Park, K.; Kim, J.-Y.; Lim, S. J.; Oh, M.; Kuk, Y.; Park, C.; Kim, S.-J.; et al. *n*-Type nanostructured thermoelectric materials prepared from chemically synthesized ultrathin Bi_2Te_3 nanoplates. *Nano Lett.* **2012**, *12*, 640–647.

[20] Soni, A.; Shen, Y.; Yin, M.; Zhao, Y.; Yu, L.; Hu, X.; Dong, Z. L.; Khor, K. A.; Dresselhaus, M. S.; Xiong, Q. H. Interface driven energy filtering of thermoelectric power in spark plasma sintered $Bi_2Te_{2.7}Se_{0.3}$ nanoplatelet composites. *Nano Lett.* **2012**, *12*, 4305–4310.

[21] Scheele, M.; Oeschler, N.; Veremchuk, I.; Reinsberg, K.-G.; Kreuziger, A.-M.; Kornowski, A.; Broekaert, J.; Klinke, C.; Weller, H. ZT enhancement in solution–grown $Sb_{(2-x)}Bi_xTe_3$ nanoplatelets. *ACS Nano* **2010**, *4*, 4283–4291.

[22] Wagner, V.; Dolling, G.; Powell, B. M.; Landweher, G. Lattice vibrations of Bi_2Te_3. *Phys. Stat. Solidi B* **1978**, *85*, 311–317.

[23] Hong, S. S.; Kundhikanjana, W.; Cha, J. J.; Lai, K.; Kong, D.; Meister, S.; Kelly, M. A.; Shen, Z.-X.; Cui, Y. Ultrathin topological insulator Bi_2Se_3 nanoribbons exfoliated by atomic force microscopy. *Nano Lett.* **2010**, *10*, 3118–3122.

[24] Teweldebrhan, D.; Goyal, V.; Balandin, A. A. Exfoliation and characterization of bismuth telluride atomic quintuples and quasi-two-dimensional crystals. *Nano Lett.* **2010**, *10*, 1209–1218.

[25] Cheng, P.; Song, C. L.; Zhang, T.; Zhang, Y. Y.; Wang, Y. L.; Jia, J.-F.; Wang, J.; Wang, Y. Y.; Zhu, B.-F.; Chen, X.; et al. Landau quantization of topological surface states in Bi_2Se_3. *Phys. Rev. Lett.* **2010**, *105*, 076801.

[26] Kong, D. S.; Dang, W. H.; Cha, J. J.; Li, H.; Meister, S.; Peng, H. L.; Liu, Z. F.; Cui, Y. Few-layer nanoplates of Bi_2Se_3 and Bi_2Te_3 with highly tunable chemical potential. *Nano Lett.* **2010**, *10*, 2245–2250.

[27] Dang, W. H.; Peng, H. L.; Li, H.; Wang, P.; Liu, Z. F. Epitaxial heterostructures of ultrathin topological insulator nanoplate and graphene. *Nano Lett.* **2010**, *10*, 2870–2876.

[28] Li, H.; Cao, J.; Zheng, W. S.; Chen, Y. L.; Wu, D.; Dang, W. H.; Wang, K.; Peng, H. L.; Liu, Z. F. Controlled synthesis of topological insulator nanoplate arrays on mica. *J. Am. Chem. Soc.* **2012**, *134*, 6132–6135.

[29] Lee, C. H.; He, R.; Wang, Z. H.; Qiu, R. L. J.; Kumar, A.; Delaney, C.; Beck, B.; Kidd, T. E.; Chancey, C. C.; Sankaran, R. M.; et al. Metal-insulator transition in variably doped $(Bi_{1-x}Sb_x)_2Se_3$ nanosheets. *Nanoscale* **2013**, *5*, 4337–4343.

[30] Min, Y.; Moon, G. D.; Kim, B. S.; Lim, B.; Kim, J.–S.; Kang, C. Y.; Jeong, U. Quick, controlled synthesis of ultrathin Bi_2Se_3 nanodiscs and nanosheets. *J. Am. Chem. Soc.* **2012**, *134*, 2872–2875.

[31] Peng, H. L.; Dang, W. H.; Cao, J.; Chen, Y. L.; Wu, D.; Zheng, W. S.; Li, H.; Shen, Z.-X.; Liu, Z. F. Topological insulator nanostructures for near–infrared transparent flexible electrodes. *Nat. Chem.* **2012**, *4*, 281–286.

[32] Yan, Y.; Liao, Z.-M.; Zhou, Y.-B.; Wu, H.-C.; Bie, Y.-Q.; Chen, J.-J.; Meng, J.; Wu, X.-S.; Yu, D.-P. Synthesis and quantum transport properties of Bi_2Se_3 topological insulator nanostructures. *Sci. Rep.* **2013**, *3*, 1264.

[33] Blake, P.; Hill, E. W.; Neto, A. H. C.; Novoselov, K. S.; Jiang, D.; Yang, R.; Booth, T. J.; Geim, A. K. Making graphene visible. *Appl. Phys. Lett.* **2007**, *91*, 063124.

[34] Zhao, Y. Y.; Chua, K. T. E.; Gan, C. K.; Zhang, J.; Peng, B.; Peng, Z. P.; Xiong, Q. H. Phonons in Bi_2S_3 nanostructures: Raman scattering and first-principles studies. *Phys. Rev. B* **2011**, *84*, 205330.

[35] Utama, M. I. B.; Peng, Z. P.; Chen, R.; Peng, B.; Xu, X. L.; Dong, Y.; Wong, L. M.; Wang, S. J.; Sun, H. D.; Xiong, Q. H. Vertically aligned cadmium chalcogenide nanowire arrays on muscovite mica: A demonstration of epitaxial growth strategy. *Nano Lett.* **2010**, *11*, 3051–3057.

[36] Zhang, J.; Peng, Z. P.; Soni, A.; Zhao, Y. Y.; Xiong, Y.; Peng, B.; Wang, J. B.; Dresselhaus, M. S.; Xiong, Q. H. Raman spectroscopy of few-quintuple layer topological insulator Bi_2Se_3 nanoplatelets. *Nano Lett.* **2011**, *11*, 2407–2414.

[37] Zhao, Y. Y.; Luo, X.; Li, H.; Zhang, J.; Araujo, P. T.; Gan, C. K.; Wu, J.; Zhang, H.; Quek, S. Y.; Dresselhaus, M. S.; et al. Interlayer breathing and shear modes in few-trilayer MoS_2 and WSe_2. *Nano Lett.* **2013**, *13*, 1007–1015.

[38] Li, Z. G.; Qin, Y. Y.; Mu, Y. W.; Chen, T. S.; Xu, C. H.; He, L. B.; Ding, W. F.; Wan, J. G.; Song, F. Q.; Han, M. et al. Visualizing topological insulating Bi_2Te_3 quintuple layers on SiO_2-capped Si substrates and its contrast optimization. *J. Nanosci. Nanotechnol.* **2011**, *11*, 7042–7046.

[39] Jung, I.; Pelton, M.; Piner, R.; Dikin, D. A.; Stankovich, S.; Watcharotone, S.; Hausner, M.; Ruoff, R. S. Simple approach for high-contrast optical imaging and characterization of graphene–based sheets. *Nano Lett.* **2007**, *7*, 3569–3575.

[40] Palik, E. D. *Handbook of Optical Constants of Solids*; Elsevier Science & Tech, 1985.

[41] Greenaway, D. L.; Harbeke, G. Band structure of bismuth telluride, bismuth selenide and their respective alloys. *J. Phys. Chem. Solids* **1965**, *26*, 1585–1604.

[42] Aspnes, D. E.; Studna, A. A. Dielectric functions and optical parameters of Si, Ge, GaP, GaAs, GaSb, InP, InAs, and InSb from 1.5 to 6.0 eV. *Phys. Rev. B* **1983**, *27*, 985–1009.

[43] Cheng, L. N.; Chen, Z.-G.; Yang, L.; Han, G.; Xu, H.-Y.; Snyder, G. J.; Lu, G.-Q.; Zou, J. T-shaped Bi_2Te_3–Te heteronanojunctions: Epitaxial growth, structural modeling, and thermoelectric properties. *J. Phys. Chem. C* **2013**, *117*, 12458–12464.

[44] Mineralogy Database. http://webmineral.com/) [Online] (accessed on 26 April, 2014)

[45] Wang, W. S.; Goebl, J.; He, L.; Aloni, S.; Hu, Y. X.; Zhen, L.; Yin, Y. D. Epitaxial growth of shape-controlled Bi_2Te_3−Te heterogeneous nanostructures. *J. Am. Chem. Soc.* **2010**, *132*, 17316–17324.

[46] Boncheva-Mladenova, Z.; Pashinkin, A. S.; Novoselova, A. V. Determination of the saturated vapor pressure of solid bismuth telluride. *Inorg. Mater. Engl. Transl.* **1968**, *4*, 241.

[47] Gorbov, S. I.; Krestovnikov, A. N. Thermodynamic properties of the gaseous chalcogenides of group V elements. *Russ. J. Phys. Chem.* **1966**, *40*, 505–507.

[48] Kashkooli, I. Y.; Munir, Z. A. The equilibrium and free surface sublimation pressures of oriented single crystals of bismuth telluride. *J. Electrochem. Soc.* **1970**, *117*, 248–250.

[49] Brebrick, R.; Smith, F. Partial and total vapor pressures over molten Bi_2Te_3. *J. Electrochem. Soc.* **1971**, *118*, 991–996.

[50] Elliott, R. P. *Constitution of Binary Alloys, First Supplement*; McGraw–Hill Company: New York, 1965.

[51] Grillo, V.; Rossi, F. STEM_CELL: A software tool for electron microscopy. Part 2 analysis of crystalline materials. *Ultramicroscopy* **2013**, *125*, 112–129.

[52] Levi, A. C.; Kotrla, M. Theory and simulation of crystal growth. *J. Phys.: Condens. Matt.* **1997**, *9*, 299.

[53] Medlin, D.; Ramasse, Q.; Spataru, C.; Yang, N. Structure of the (0001) basal twin boundary in Bi_2Te_3. *J. Appl. Phys.* **2010**, *108*, 043517.

[54] Medlin, D. L.; Yang, N. Y. C. Interfacial step structure at a (0001) basal twin in Bi_2Te_3. *J. Electron. Mater.* **2012**, *41*, 1456–1464.